Electrochimica Acta 247 (2017) 958–969

Contents lists available at ScienceDirect

Electrochimica Acta

journal homepage: www.elsevier.com/locate/electacta

# Tuning the Oxygen Reduction Activity and Stability of $Ni(OH)_2$@Pt/C Catalysts through Controlling Pt Surface Composition, Strain, and Electronic Structure

Fernando Godínez-Salomón[a,b,*], Christopher P. Rhodes[b,*], K. Suarez Alcantara[c], Qiushi Zhu[d], S.E. Canton[e,f], H.A. Calderon[g], J.L. Reyes-Rodríguez[a], M.A. Leyva[a], O. Solorza-Feria[a,*]

[a] Departamento de Química, Centro de Investigación y de Estudios Avanzados del IPN, Mexico City, Mexico
[b] Department of Chemistry and Biochemistry, Texas State University, 601 University Dr., San Marcos, TX, 78666, USA
[c] Unidad Morelia del Instituto de Investigaciones en Materiales-UNAM. Antigua carretera a Pátzcuaro 8701, Col. Ex-hacienda de San José de la Huerta, Morelia, Michoacán, 58190, Mexico
[d] Center for Ultrafast Imaging, University of Hamburg, 22761 Hamburg, Germany
[e] FS-SCS, Deutsches Elecktronen-Synchrotron (DESY), Notkestr. 85, 22607, Hamburg, Germany
[f] Max Planck Institute for Biophysical Chemistry, Am Fassberg 11, 37077, Göttingen, Germany
[g] Departamento de Física, ESFM-IPN, Ed. 9, UPALM-Zacatenco, México D.F, Mexico

ARTICLE INFO

*Article history:*
Received 1 February 2017
Received in revised form 12 June 2017
Accepted 13 June 2017
Available online 15 June 2017

*Keywords:*
Core-shell nanoparticles
oxygen reduction
fuel cells
lattice strain
electronic effect

ABSTRACT

Nanoparticles of $Ni(OH)_2$ surrounded with ultra-low Pt content and supported on functionalized carbon were prepared by a scalable synthesis method and investigated as electrocatalysts for the oxygen reduction reaction (ORR) in acidic media. The effect of altering the Pt surface composition on the $Ni(OH)_2$ nanoparticle core was investigated as a route to simultaneously increase the ORR activity and stability. Modifying the Pt surface composition resulted in both structural and electronic changes. Decreasing the Pt surface composition resulted in stronger Pt-Pt compressive strain and decrease in the occupancy of d-band vacancies per atom. The correlation of strain and d-vacancies with ORR activity and stability showed a Volcano-type tendency, with the 6 wt. % Pt sample showing the highest activity and stability. The electrochemical results obtained using rotating disk electrode (RDE) tests showed an enhancement of about six times higher surface and mass-normalized activity as well as improved durability compared to commercial Pt/C. These improvements were further corroborated by single cell membrane electrode assembly (MEA) tests where similar trends were observed, showing higher power densities with lower Pt loadings, in comparison with commercial Pt/C. These results show that new electrocatalysts with higher activity and stability can be obtained through precise control of the atomic-level catalyst structure.


## 1. Introduction

The identification and design of novel nanocatalysts that provide improved oxygen reduction activity and stability at lower cost, remains a key challenge for electrochemical energy conversion and storage devices including fuel cells, metal-air batteries, and electrolyzers [1,2]. In particular, proton-exchange membrane fuel cells (PEMFCs) efficiently convert diverse fuels into electricity and are key components in the development of a reliable, safe, and sustainable clean energy economy. However, the performance PEMFCs is substantially compromised by the sluggish oxygen reduction reaction (ORR) kinetics which impose the use of higher catalysts loadings (*i.e.* Pt) at the cathode side thereby increasing fuel cell costs [3]. To enable the widespread production of commercially affordable PEMFC vehicles, performance and cost targets have been put forth by agencies such as the U.S. Department of Energy (DoE) and the Japanese New Energy and Industrial Technology Development Organization (NEDO) [4]. For instance, the US DoE 2017 technical targets for PEMFC cathodes are a Pt-based mass activity of $>0.44\ A\ m_{Pt}^{-1}$ at 0.9 V, catalyst loading of $0.125\ mg_{PGM}\ cm^{-2}$ (PGM: Pt group metal), cost per power of $\$15\ kW^{-1}$, and stability target of <40% loss in catalytic activity after 5000 h of operation.

* Corresponding authors.
*E-mail addresses:* cprhodes@txstate.edu (C.P. Rhodes), osolorza@cinvestav.mx (O. Solorza-Feria).

http://dx.doi.org/10.1016/j.electacta.2017.06.073
0013-4686/

Meeting these significant technical and cost challenges requires the development of new electrocatalysts with high activity, long durability, and lower cost through controlling atomic level structure, using simple and scalable synthesis methods, understanding and mitigating degradation mechanisms, and designing catalyst layer architectures within membrane electrode assemblies (MEAs) that provide optimal performance. The use of Pt-based alloys and non-Pt catalysts have been investigated to reduce the amount of Pt contained in the catalyst layer of the MEA [5]. Recent synthetic advances have allowed the formation of nanoparticles (NP) with precise control of size, shape, composition, and structure [6–8], however, many synthetic approaches are possible only at low scale.

Recently, core-shell nanoparticles have received significant attention as an approach to reduce Pt loading and obtain high activity and stability. Core-shell architectures consist of an alloy or pure metal core with a Pt-enriched nanoparticle shell. The core-shell approach provides very low noble-metal loading and altered electronic properties, which can modify adsorption/desorption processes within the oxygen reduction reaction and improve the electrocatalytic performance [9,10]. Previous work have shown that using core-shell nanoparticles can result in significant activity and durability improvements as well as reduced catalyst cost [10,11]. Core-shell structures have the potential to meet and even exceed the activity target for the automotive industry [12]. However, further advances are needed to provide scalable and cost-effective synthetic approaches able to determine the effect of composition on performance, in order to improve the long-term durability.

Previous work has examined the ORR activity of carbon-supported Pt-M alloys (M = non-noble transition metal) [13]. Core-shell Ni/Pt nanoparticles have been studied, and prior work showed the importance of the Ni:Pt ratio on the ORR electrocatalytic activity [14]. The activity of oxygen reduction electrocatalysts can be tuned by changing the transition metal composition to alter the surface electronic structure as supported by previous work [15]. Further, obtaining surface-segregated Pt that forms Pt "skin" structure with sub-surface Ni has been shown to significantly increase ORR activity [16].

Scalable synthesis methods that allow the formation of nanoparticles that contain surface-segregated Pt with sub-surface Ni are of significant interest. Despite several efforts on synthesizing metallic Pt-M alloys dealing with the presence of surface oxides is key challenge [17]. For synthesis methods that involve aqueous solutions, using a metallic Ni nanoparticle core and depositing Pt onto the surface metallic Ni is particularly problematic since hydroxide/oxide species form at the surface of metallic Ni [18]. Metallic Ni surfaces have been shown to passivate and form oxide/hydroxide layers when cycled to positive potentials under acidic conditions [19]. The formation of surface oxide/hydroxide species is a particular challenge for Ni nanoparticles due to its implication on physiochemical properties [20].

In this work, we report the effects of altering the Pt surface composition on $Ni(OH)_2$ nanoparticle cores which was investigated as a route to simultaneously increase the ORR activity and stability. To our knowledge, the effect of surface composition of Pt on Ni-based core-shell nanoparticles on both the activity and stability has not been significantly investigated. To enable surface-segregated Pt within a scalable aqueous-based synthesis method, Pt was deposited onto $Ni(OH)_2$ nanoparticles due to the inevitable formation of Ni oxides/hydroxides within aqueous solutions. Although by itself $Ni(OH)_2$ is well known to be unstable in acidic conditions [21], a Pt shell or skin structure has been shown to stabilize subsurface transition metals [22,23]. Further, Ni interaction with Pt has been shown to be stabilize Ni within the structure within acidic conditions over extended cycles [24,25].

The surface composition of Pt can alter the electroactivity and stability due to changes in the nature of surface Pt-M interactions. Toward this end, we investigated the optimization of the intrinsic electrochemical properties of carbon-supported $Ni(OH)_2$@Pt/C structures based on tuning the electroactivity and stability for the ORR through modifying the Pt content on the surface. The electrochemical ORR activity and stability was obtained by using rotating disk electrode experiments, and single cell MEA fuel cell tests. Our work shows that both the catalyst activity and the stability are significantly affected by the Pt surface composition, and these changes were induced by changes in the atomic-level geometry and electronic structure.

## 2. Experimental

### 2.1. Carbon functionalization

Carbon (1.5 g, Vulcan XC-72R) was used as starting material and was thermally treated under a hydrogen atmosphere at 500 °C for 2 hours to remove impurities. Then, 600 mg of the $H_2$-treated carbon was dispersed in 100 mL of 20 v/v % $HNO_3$, stirred in an ultrasonic bath for 1 hour at room temperature, and then boiled for 1 hour. The carbon was recovered by centrifugation at 15,000 rpm, washed several times with a mixture 1:1 of ultrapure water and acetone, and then dried in a $N_2$ flow at 100 °C for 2 h. In a second step, a fraction of 260 mg of prior treated carbon was dispersed in 50 mL of water with 1.83 mL of ethanolamine. The slurry was sonicated, boiled for 2 hours, recovered, and then washed and dried as described above.

### 2.2. Synthesis of electrocatalysts

The carbon supported $Ni(OH)_2Pt$/C-*x* electrocatalysts were prepared using a modified two step procedure previously reported [26]. Briefly, $Ni(NO_3)_2.6H_2O$ (423 mg, 1.45 mmol), tetrabutylammonium bromide (470 mg, 1.45 mmol) and the functionalized carbon (200 mg, 70 wt.% with respect to metallic Ni content) were dispersed in 70 mL of ethanol. The suspension was stirred in an ultrasonic bath for 10 minutes and then transferred into a reflux system. After bubbling $N_2$ and magnetically stirring for 20 minutes, $NaBH_4$ (124 mg, 0.258 mmol) dissolved in 20 mL of ethanol was slowly dropped into the solution at room temperature and allowed react during 1 hour. Then, 10 mL of MQ-water was added to eliminate the excess $NaBH_4$. The Pt deposition was carried out by adding an appropriate amount of $K_2PtCl_6$ dissolved in 30 mL of MQ-water to obtain 10, 20 and 40 wt. % vs metallic Ni, corresponding to 3, 6 and 12 total wt. %. Upon this step, the temperature was gradually increased to 60 °C and the reaction was allowed to proceed over 4 hours. Finally, the catalyst were recovered by centrifugation and thoroughly washed with MQ-water and ethanol. The powder was dried for two hours at 150 °C under CO atmosphere. The series of NiPt catalysts are named as $Ni(OH)_2$@Pt/C-*x* where *x* represents the total weight content of Pt, i.e. 3, 6 and 12%.

### 2.3. Physical Characterization

The catalyst composition was determined using inductively coupled plasma atomic emission spectroscopy (ICP-AES), carried out by Galbraith Laboratories Inc. The structure, particle size, morphology, and distribution of the catalysts were determined using a Cs-corrected high angle annular dark field scanning transmission electron microscopy (HAADF-STEM) obtained from a JEOL ARM 200F equipped with an energy dispersed spectrometer (EDAX Silicon Drift detector). Selected area electron diffraction (SAED) was obtained from a 2010-F (200 kV, JEOL). Low-dose

transmission electron microscopy (LD-TEM) was carried out using an aberration corrected: C5, C3, A1, A2 and A3, TEAM 0.5 microscope with spatial resolution below 0.06 nm and current density around 5-10 attoA/Å$^2$s. Further details are reported elsewhere [27]. XRD measurements were obtained with a PANALYTICAL instrument using Kα Cu: 1.54056 Å. The phases (*i.e.* $Ni(OH)_2$, Pt, Ni, and graphite) were assigned with lattice parameters, spatial groups, and atomic positions obtained from the Inorganic Crystal Structure Database (ICSD). The experimental XRD patterns were fitted and analyzed using Rietveld refinement using Topas academic v.4.2. The validity of the fit was assessed by the low value of the "goodness of fit number" (GOF) and the presence of Pt within the samples was further validated by additional characterization methods, as described in the text.

X-ray Absorption Spectroscopy (XAS) spectra were taken at the I811 beamline of MAX-Lab synchrotron facility, Sweden [28,29] over different runs according to the edge energy. XAS spectra were recorded at the Ni K-edge, Pt $L_3$-edge, and Pt $L_2$-edge in Fluorescence mode. A Lytle detector was used with the appropriate filter, i.e. Zn for Pt and Co for Ni. 5 scans collected and averaged. The scans were taken between −200 eV and 1000 eV with respect to the edge energy. The estimation of the d-band vacancies was carried out using a method proposed by Murkerjee et al. [30], based on the integration of the XANES signal around the $L_3$ and $L_2$-edges of Pt as follows:

$$(h_J)_{total,sample} = (1.0 + f_d)(h_J)_{total,reference} \quad (1)$$

Where the $h_J$ is the total number of unoccupied d-states per atom; the $h_J$ for Pt pure was estimated as 0.3 [30] and is our material of reference (Pt foil). $f_d$ is the fractional change of d-vacancies relative to the reference material; it is described as:

$$f_d = \frac{\Delta A_3 + 1.11\Delta A_2}{(A_3 + 1.11A_2)_{reference}}, \quad (2)$$

$$\Delta A_3 = A_{3,sample} - A_{3,reference}, \quad (3)$$

and

$$\Delta A_2 = A_{2,sample} - A_{2,reference}, \quad (4)$$

$A_3$ and $A_2$ refer to the integrated area between −10 eV and +13 eV, above and below, the Pt $L_3$ and $L_2$ edges at the samples and reference.

### 2.4. Rotating Disk Electrochemical characterization

The electrochemical measurements were conducted at constant temperature (298 K) in a three electrode cell using a rotating disk electrode (RDE) setup and potentiostat/galvanostat (PARSTAT model 2273). A Pt mesh and a freshly prepared reversible hydrogen electrode (RHE) were used as counter and reference electrodes respectively. A glassy carbon used as working electrode (0.196 cm$^2$), was prepared by suspending proper catalysts powder in aqueous Nafion® solution, following procedures previously reported [31]. To avoid undesired catalyst modification and improve reproducibility, the working electrode was immersed into the electrochemical cell under potential control at 0.1 V. The catalyst was then cycled several times (30 scans) up to 1.2 V to obtain a stable voltammogram, referred to as "activation step". After the activation step, the electrolyte was replaced with a fresh 0.1 M $HClO_4$ solution for further analysis. The Pt loading was earlier optimized depending on catalysts (i.e. 10–25 μg cm$^{-2}$) [32]. IR-compensation and background subtraction were considered to obtain electrochemical parameters. The electrochemical surface area was calculated by CO-stripping, considering 420 μC cm$^{-2}$ as the charge corresponding to a monolayer of adsorbed CO. The results were compared with that of a commercial Pt/C catalyst.

### 2.5. Membrane Electrode Assembly (MEA) Fabrication and Testing

The cathode catalyst ink was prepared according to the following procedure: *i*) an appropriate amount of the catalyst was blended with 0.5 mL of MQ-water and sonicated for 20 seconds and then magnetically stirred at 5 °C for 24 h. *ii*) a Nafion® solution (5 wt%) was added in order to obtain 30 wt.% in relation to the total catalyst loading. The slurry was maintained for 24 h more at the same conditions (*i.e.* 5 °C under stirring). *iii*) Finally, 0.5 mL of propanol was added, stirred for 4 h at 5 °C, and then was immediately used for the MEA preparation. The casting was carried out using catalyst coated substrate (CCS) method by brushing the ink onto a gas diffusion layer (GDL,Sigraset 25BC), followed by drying at 80 °C for three minutes. The process was repeated until a total of Pt loading of ~0.1 mg cm$^{-2}$ for Pt/C (E-tek) and 0.05 mg cm$^{-2}$ for $Ni(OH)_2$@Pt/C-6 and $Ni(OH)_2$@Pt/C-12 was obtained. The catalyst loading was calculated by weighting GDL before and after ink deposition. A commercial catalyzed GDL (20 wt.% Pt/C, 0.5 mg cm$^{-2}$ Pt) was used as the anode. The anode and cathode gas diffusion catalysts (GDC) were hot-pressed at both sides of a Nafion® membrane (1135, ~84 μm) at 120 °C and at 4.4 kgf cm$^{-2}$ for 120 s. The fuel cell performance was evaluated in a 5 cm$^2$ single cell using a fuel cell test system 890e multi-range. The catalyst mass activity (MA) and polarization studies were performed under $H_2/O_2$, at 80 °C and ~ 80% relative humidity (RH).

## 3. Results and discussion

### 3.1. Approach for $Ni(OH)_2$@Pt/C-x nanoparticles

A set of bimetallic electrocataysts $Ni(OH)_2$@Pt/C-*x*, with different platinum content (*x* = 3, 6 and 12 wt. %) and supported on functionalized amorphous carbon (70 wt. %), were synthesized using a simple bottom up procedure consisting of a Ni-precursor reduced with sodium borohydride and a subsequent trans-metallation reaction with the Pt precursor (see experimental section). As further described below, the synthesis procedure produced a high yield, well controlled elemental ratio, narrow particle size distribution, and high dispersion. The Pt content was varied in order to optimize the electrocatalytic performance and stability toward the ORR based on tuning the Pt geometry and electronic structure, induced by interaction with the $Ni(OH)_2$. Furthermore, the surface of the carbon support was modified by anchoring ethanolamine in order to improve the adsorption properties and create nucleation sites that promote narrow size distribution and well-dispersed nanoparticles, which are critical factors for obtaining superior electrochemical performance [33].

### 3.2. Physical characterization

The morphology, distribution, chemical composition and structure of supported $Ni(OH)_2$@Pt/C-*x* catalysts was determined using scanning transmission electron microscopy (STEM) and x-ray diffraction (XRD). Fig. 1a and b shows representative low resolution STEM images and their corresponding particle size distributions, before and after electrochemical stability tests. The as-prepared catalysts (Fig. 1a) showed similar particle size (*ca.* 2–3 nm), high particle density, and good distribution on the carbon support. Narrow size distribution and low degree of aggregation minimizes the contribution of particle size effects on the electrochemical analysis thereby allowing direct comparison among the catalysts [34]. Unlike the commercial Pt/C sample, the functionalized amorphous carbon used as support of the Ni

$(OH)_2$@Pt/C-*x* catalysts showed sheet-like features. The graphene-like morphology was created through chemical exfoliation of the carbon layers during the functionalization process [35]. After the electrochemical stability test (i.e. 5000 cycles from 0.6 to 1.1 V/RHE), an increase in the particle size and number of agglomerates was observed (Fig. 1b). Previous reports have proposed several factors including particle migration, Pt-dissolution and redeposition (Ostwald ripening), and carbon corrosion as contributors to this phenomenon [36]. Regarding the carbon support, the nano-sheet-like features were no longer observed, which indicates that a corrosion process occurs on the support material. In order to obtain better insight into the structure of the catalysts, High-resolution STEM, energy-dispersive x-ray spectroscopy (EDS), selected area electron diffraction (SAED) (Fig. S1) and low dose TEM (LD-TEM) (Fig. 2), were carried out. In summary, all the techniques support the formation of a Pt enriched surface and changes in the structure related with elements interaction. From SAED (Fig. S1a), the lattice plane distance depended on the Pt content. The presence of Ni $(OH)_2$ was also detected. The EDS analysis (Fig. S1c) carried out on randomly chosen single nanoparticles (Fig. S1b) show well distributed Ni:Pt with strong Ni-Pt interactions. It is important to mention that during STEM analysis, changes in the particle shape, atomic reconstruction and even atomic detaching were commonly observed due to the high beam energy used for the STEM analysis (Fig. S2) [27]. Using LD-TEM, allows better observation of the structure without damaging the nanoparticles [27]. The reconstructed exit wave function (Fig. 2a–c) exhibited consistently high surface segregated Pt, and this coverage increased with the Pt content. The Ni$(OH)_2$@Pt/C-3 sample showed an incomplete Pt surface layer was formed (Fig. 2a, labeled with

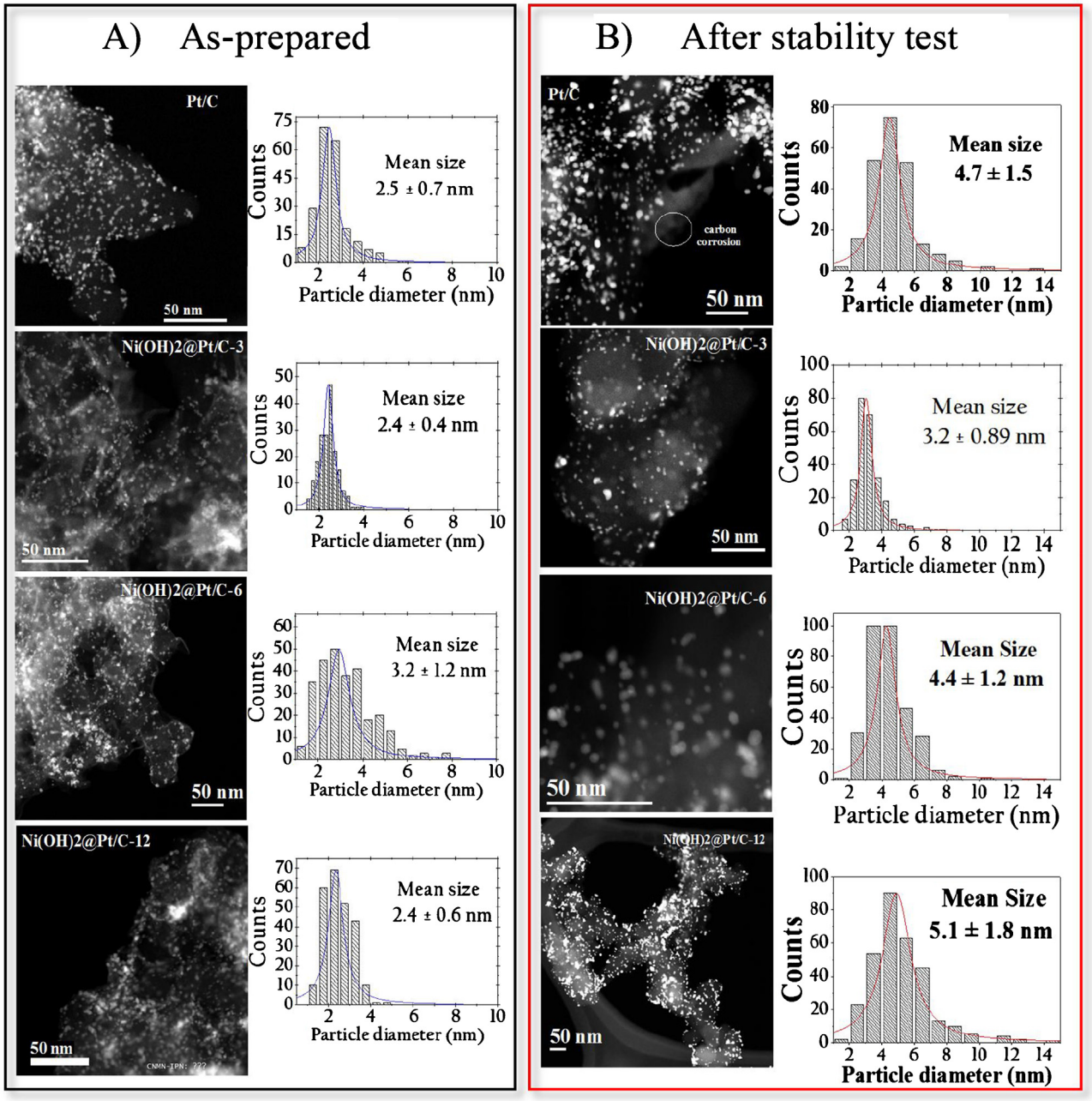


**Fig. 1.** Low resolution STEM micrographs and particle size distribution histograms, before (a) and after stability test (b). The stability test was carried out in $N_2$-saturated 0.1 M $HClO_4$ between 0.6 and 1.1 V during 5 000 cycles.

arrows). This result agrees with the results obtained by electrochemistry, where a small peak associated with oxidation of Ni-species was detected (see below). The $Ni(OH)_2$@Pt/C-6 and $Ni(OH)_2$@Pt/C-12 samples (Fig. 2b–c) showed more consistent Pt coverage. Island growth patterns with more than one Pt monolayer were also observed on the $Ni(OH)_2$@Pt/C-12 sample (Fig. 2c). This observation can be explained by the differences in bonding energies between Pt-Pt and Pt-O-Ni, which would lead to an island growth pattern for the deposited Pt since the newly formed Pt layer tended to adhere to other Pt layers, rather than interacting with the $Ni(OH)_2$ surface. Similar results were found by theoretical studies on Ni@Pt catalysts carried out in our group [37]. Although a quantitative determination of the particle size was not feasible due to the small area analyzed with LD-TEM, the presence of smaller clusters close to each other were seen scattered throughout the sample unlike STEM. This observation is in agreement with surface reconstruction and particle coagulation observed during STEM analysis [27]. These results along with XRD and electrochemical evidences, supported the presence of high Pt-enriched surface nanostructure.

Fig. 3 shows the experimental (black line) and Rietveld-fitted (blue line) X–ray diffraction patterns of $Ni(OH)_2$@:Pt/C-*x* catalysts, commercial Pt/C (Etek®) and $Ni(OH)_2$/Ni nanoparticles used as reference. The experimental XRD, and fitting from refinement, and peak assignments are shown in Fig. S3A-C. The $Ni(OH)_2$/Ni sample consisted of a mixture of two different nanoparticles identified as

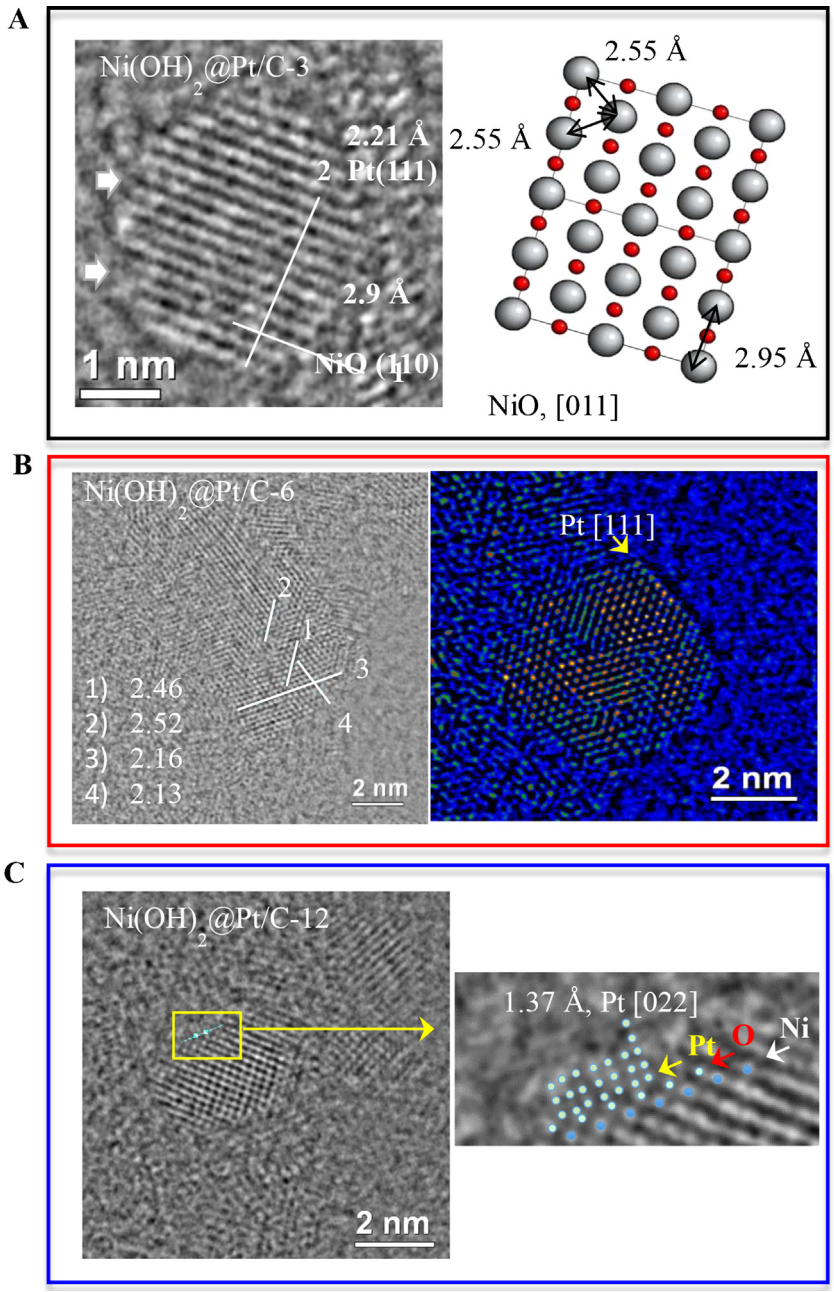


**Fig. 2.** Phase images after electron wave reconstruction from LDR-ATEM of (A) Ni(OH)2@Pt/C-3 nanoparticles (dose rate 60 $e^{-}Å^2s$); (B) $Ni(OH)_2$@Pt/C-6 (dose rate 19 $e^{-}Å^2s$); and (C) $Ni(OH)_2$@Pt/C-12 (dose rate 35 $e^{-}Å^2s$). On sample $Ni(OH)_2$@Pt/C-12 was possible to detect small island (inset top-right) of many layer of Pt. Outer layer trends to lattice relaxation toward bulk Pt parameters.

metallic Ni (PDF-04-0850) and a highly disordered α-Ni(OH)$_2$ (PDF-38-0715). The diffraction patterns of the as-prepared electrocatalysts (Ni(OH)$_2$@Pt/C-*x*) exhibit reflections of Pt and Ni(OH)$_2$ with face cubic centered (fcc) and hexagonal close-packed (hcp) structures respectively. Clearly, all three synthesized catalysts show diffraction lines for Pt that are shifted to higher 2Θ values, indicating a distortion of the Pt-lattice due to interaction with α-Ni(OH)$_2$. These results suggest that atomic strain within the Pt phase is promoted by a strong interaction which could be due to interaction of Pt with Ni(OH)$_2$ (i.e. Pt-O-Ni), surface tension effects [38], or Pt-Ni alloy formation. Depending on the Pt composition, the lattice parameter associated with the platinum is shorter than bulk Pt: 3.814 Å (Ni(OH)$_2$:Pt/C-3), 3.866 Å (Ni(OH)$_2$@Pt/C-6), 3.877 Å (Ni(OH)$_2$@Pt/C-12), and 3.923 Å (Pt/C-Etek). The occurrences of multiple diffraction lines results from the presence of different structures (i.e. Ni(OH)$_2$ and Pt), and could be related to different factors such as (i) geometrical isomers [39–42] or (ii) presence of isolated particles of different materials (i.e. Pt and α-Ni(OH)$_2$), such as the sample Ni/Ni(OH)$_2$ used as reference. The presence of isolated nanoparticles of Ni(OH)$_2$ and/or Pt was discarded by elemental analysis using STEM-EDS over several particles randomly selected (Fig. S1), which show homogeneous distribution of the elements Ni/Pt with strong interactions. Then, in conjunction with microscopy, the presence of segregated phases is attributed to the presence of a heterostructure Ni(OH)$_2$/Pt, with a high Pt surface segregation [43].

### 3.3. X-ray absorption spectroscopy

To elucidate the electronic and local structure of the nanoparticles, X-ray absorption spectra (XAS) were recorded at the Ni K-edge as well as at the Pt $L_3$-edge and Pt $L_2$-edge. The first derivative of the normalized μ(E) data is also presented at the inset of Fig. 4a and c. Fig. 4a shows the XAS at the Ni K-edge. The Ni foil (orange line) used as reference for the energy calibration represents the absorption edge at 8333 eV followed by multiple and scattering events at higher photon energy [44]. Comparing Ni-foil and nanoparticulate samples revealed remarkable differences: (i) the appearance of a small pre-edge signal, at roughly 8331 e, (ii) a shift of the K-edge position towards higher energies (8345 eV), and (iii) an evident increase of the intensity of the white-line peak as compared to metallic Ni. These differences are due to different coordination environments as further supported by the analysis of the X-ray Absorption Fine Structure (EXAFS) region using the phase corrected amplitude of the Fourier transform of the k3-weigthed signal ($k^3\chi(k)$) (Fig. 4b and d). The orange line corresponding to the Ni foil showed two peaks, related with the first and second coordination shells of Ni-Ni bond distances in metallic Ni, at 2.42 Å and 3.51 Å respectively. These values agree with the values reported for metallic Ni of Fm–3 m symmetry, 41508-ICSD. On the other hand, the synthesized catalysts showed peaks at 1.92 Å and 2.83 Å for the first and second coordination shell respectively, which fit with Ni-O bond distances of $NiO_2$ (R-3mH, 78698-ICSD). In summary, all the spectral features from the Ni(OH)$_2$@Pt/C-*x*

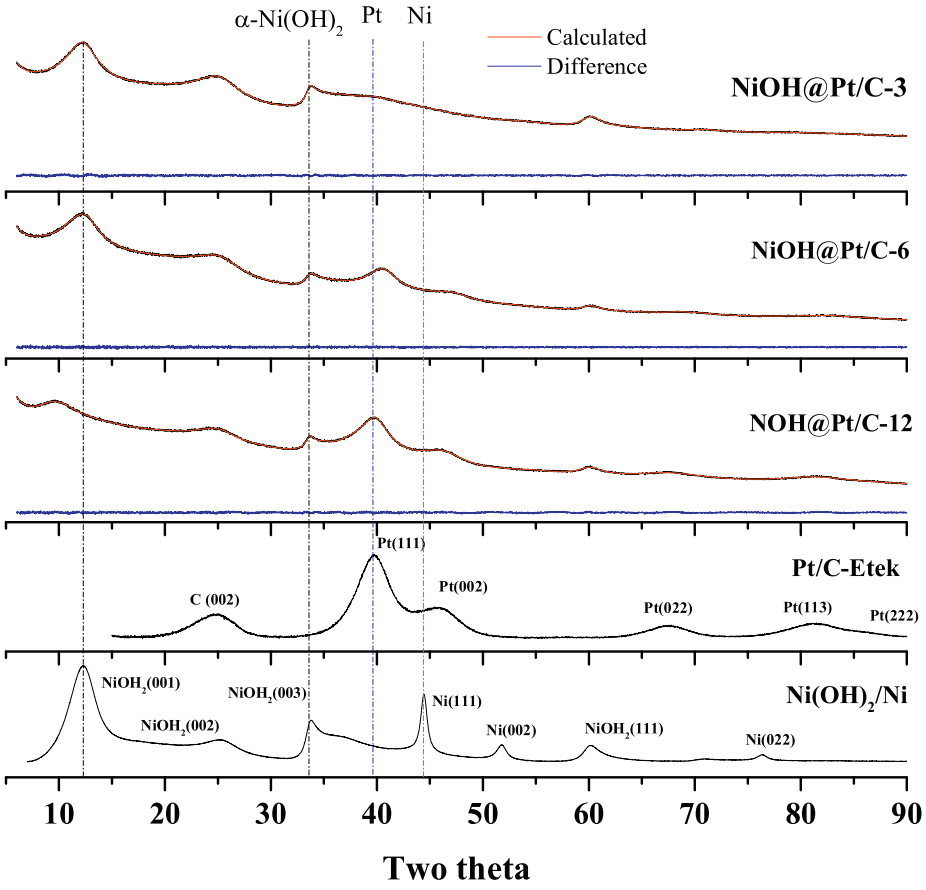


**Fig. 3.** Powder X-ray diffraction (XRD) patterns of as synthesized Ni(OH)$_2$@Pt$_x$/C nanoparticle catalysts. XRD of Pt/C-Etek and Ni(OH)$_2$/Ni core are taken as references. Red and blue lines represent fitted pattern through Rietveld analysis and statistical difference respectively.

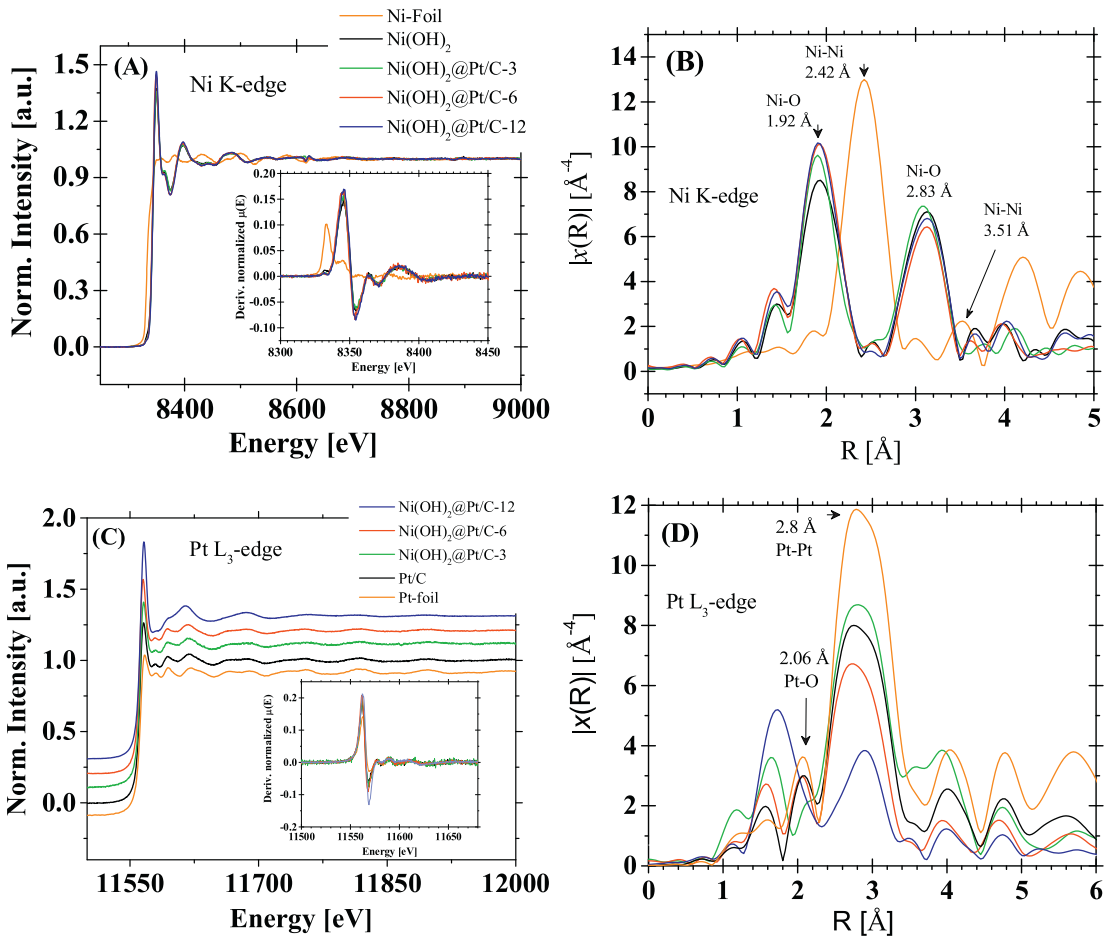


**Fig. 4.** (A) X-ray absorption near edge structure at the Ni Ni K-edge (8333 eV) and Pt $L_3$-edge (11564 eV) for the as-prepared $Ni(OH)_2$@Pt/C-*x* catalysts and Ni/$Ni(OH)_2$ and commercial Pt/C as reference Ni and Pt foil were used for calibration. The insets correspond to the first derivative of the normalized μ(E) data.

samples were consistent with nickel oxides rather than metallic Ni. Fig. 4c presents the XAS signal at the Pt $L_3$-edge. The $L_3$ and $L_2$ edges (not shown) are due to excitations of $2p_{1/2}$ and $2p_{3/2}$ electrons to empty states in the vicinity of the Fermi levels (i.e. the 5d-band) [45]. The Pt $L_3$-edge is situated at 11564 eV, while the Pt $L_2$-edge is situated at 13273 eV. The inset of Fig. 4c presents the first derivative of the normalized μ(E) signal. All materials exhibited the $L_3$ and $L_2$-edges at the same energy and no pre-edge features were observed. The orange line represents a Pt foil signal used as a reference and for energy calibration. Comparing with the response from the nanoparticles, there is a continuous increase in the intensity of the white-line peak from Pt/C to $Ni(OH)_2$@Pt/C-*x* at both edges. The intensity of the $L_3$ increases with the Pt d-band vacancy and can been used for the determination of the Pt d-band

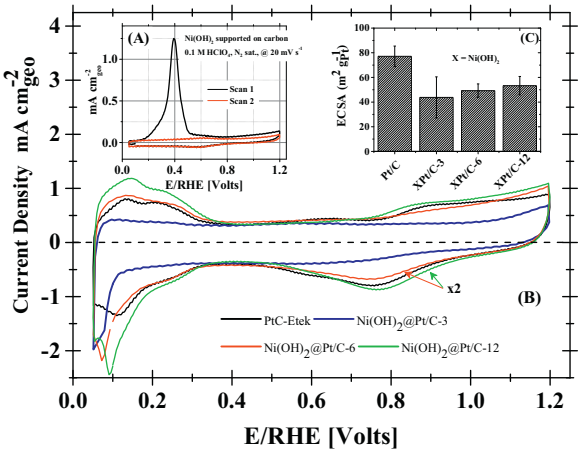


**Fig. 5.** (A) CV of $Ni(OH)_2$/C into electrochemical evaluation conditions i.e. 0.1 M $HClO_4$ electrolyte previously degassed with $N_2$. (B) Set of CV's of the $Ni(OH)_2$@Pt/C-*x* with different $Ni(OH)_2$:Pt ratio and commercial Pt/C. (C) Electrochemical surface area determined by CO-stripping considering 420 μC/$cm^2$ as the charge corresponding to a monolayer of adsorbed CO.

occupancy per atom [30]. Table S2 presents the results of the estimation of the Pt d-vacancies per atom following the method described by Mukerjee et al. [30]. EXAFS analysis of Pt $L_3$-edge between 2–4 Å for R led to the phase corrected amplitude of the Fourier transform of the k3-weighted signal ($k^3\chi(k)$) as shown in Fig. 4d. The signal at 2.06 Å can be linked to the Pt-O bond distance, estimated as 2.04 Å [46]. The peak at 2.80 Å is consistent with the Pt-Pt bond distance (reported as 2.785 Å, Pt Fm-3m, 64919-ICSD). In these main peaks, a widening after 3 Å could be consistent with the Pt-Pt bond distance on PtO (3.04 Å, PtO, P42/mmc, 4124669-COD). No indication of Pt-Ni interactions was observed [47].

### 3.4. Electrochemical Characterization

Cyclic voltammetry (CV) and CO stripping voltammetry experiments were used to determine the electrochemical surface area (ECSA) and to obtain further insight into surface structure of the nanoparticles. CVs were performed in a thermostatically controlled (298 K) 0.1 M $HClO_4$ electrolyte, previously degassed with $N_2$. As a systematic procedure, the immersion potential of the working electrode was controlled at 0.1 V/RHE, and then the electrode was cycled several times to attain a stable curve (Fig. 5b). The sample $Ni(OH)_2$/Ni supported on carbon (70 wt.%) was used as a baseline and characterized under similar conditions (Fig. 5a). As soon as voltage cycling was applied, the $Ni(OH)_2$/Ni species started to leach out (i.e. ~0.4 V vs RHE) until complete dissolution after the first cycle, owing to instability in acidic media [48]. Similar features, although a lesser extent, were observed on $Ni(OH)_2$@Pt/C-3 sample, where a small oxidation peak ~0.4 V was detected during the first scan, consistent with an incomplete coverage of Pt. In contrasts, distinct voltammetric features due to Ni leaching were not evident for $Ni(OH)_2$@Pt/C-6 and $Ni(OH)_2$@Pt/C-12 samples. Shown in Fig. 5b are potentiodynamic curves of Pt/C-Etek and Ni $(OH)_2$@Pt/C-*x* catalysts. For clarity, CVs of $Ni(OH)_2$@Pt/C-6 and Ni $(OH)_2$@Pt/C-12 were multiplied by a factor of 2. After several scans, the ubiquitous $Ni(OH)_2$ and/or surface contaminants were removed from the surface of the nanoparticles and a stable curve resembling a typical high-surface-area Pt profile was attained [49]. This initial conditioning process which could involve leaching of Ni $(OH)_2$ species was particularly important for the surface reorganization. The selective electrochemical stripping of unstable, non-noble elements, is a key process during the formation of the active catalyst [50]. Sweeping anodically (sweeping the potential towards more positive values), a small yet clear negative shift (91 mV) in the $OH_{ad}$ formation was observed on the catalyst $Ni(OH)_2$@Pt/C-12 with respect to $Ni(OH)_2$@Pt/C-6 and Pt/C. However in the reverse scanning direction, the oxide reduction peak on both $Ni(OH)_2$@Pt/C-6 and $Ni(OH)_2$@Pt/C-12 (~0.77 V) shifted toward more positive potential versus Pt/C (~0.75 V). Then, even when a higher fraction of oxygenated species could be formed, their reduction was apparently faster. The ECSA was estimated from integrating the CO-stripping charge (Fig. 5c). Similar results were obtained using $H_{upd}$ region (E < 0.4 V), which is consistent with a Pt-skeleton architecture [51] rather than Pt-skin, where a suppression of proton adsorption has been reported [52].

The calculated ECSA for the $Ni(OH)_2$@Pt/C-*x* catalysts were very similar which is consistent with the STEM results. Only a small increase of ECSA was observed with increasing the Pt content, suggesting a slightly higher percent of Pt atoms on the surface. Compared to commercial Pt/C, where a similar particle size and

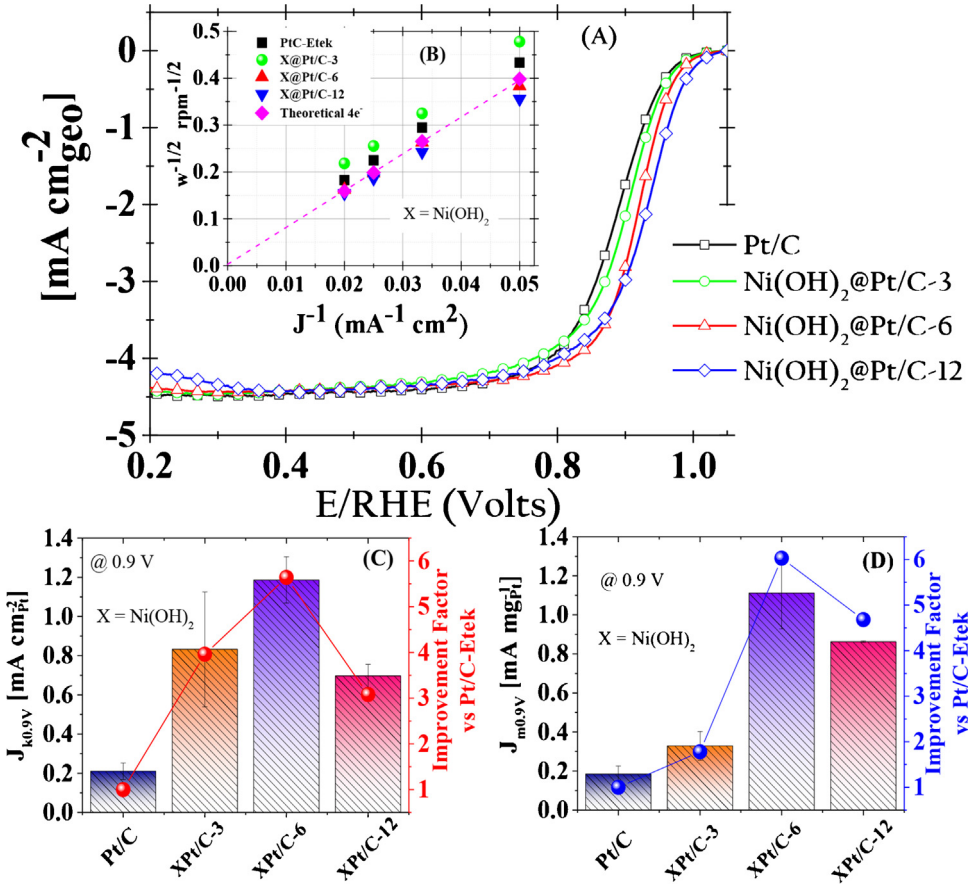


**Fig. 6.** (A) Steady-state polarization curves for the ORR on commercial Pt/C-Etek and $Ni(OH)_2$@Pt/C-*x* in $O_2$ saturated 0.1 M $HClO_4$. (B) Koutecky-Levich plot and (C and D) specific activity and mass activity after normalization.

distribution were observed by STEM (Fig. 1), the lower ECSA of Ni $(OH)_2$@Pt/C-*x* nanoparticles was attributed to the presence of Ni $(OH)_2$ species on the surface and Pt within the nanoparticles which is not electrochemically accessible [49,51].

The ORR electrocatalytic activity and stability were carried out by using the rotating disk electrode (RDE) configuration based on previous reports [31,50]. Prior to these measurements, the electrolyte was renewed with a fresh solution after the break-in conditioning step. Fig. 6a shows the potentiodynamic curves (i.e. positive-going scan) after background subtraction of the capacitive current contribution arising from the carbon support. Overall, the onset curves of Ni$(OH)_2$@Pt/C-*x* samples showed lower overpotentials compared to commercial Pt/C. A summary of the electrocatalytic properties is presented in Table 1. The experimental ECSA, Pt-mass activity, and Pt specific activity values obtained for commercial Pt/C are very consistent with the reported state-of-the-art values [53], which validates the results.

The analysis of the half-wave potential, $E_{1/2}$, (Table 1), showed positive shifting versus Pt/C of 23 mV (Ni$(OH)_2$@Pt/C-3), 38 mV (Ni $(OH)_2$@Pt/C-6), and 46 mV (Ni$(OH)_2$@Pt/C-12), respectively. Normally, shifting to more positive value on the half wave potential, $E_{1/2}$, is directly related with increasing the electrocatalytic activity. However it should be taken into account that only the geometrical area is considered at this point. Therefore, the seemingly contradictory behavior between the values of $E_{1/2}$ and the specific activity may be due to differences in the nominal Pt-loading onto the glassy carbon electrode and the concomitant inter-particle separation and corresponding layer thickness, which might influence the absolute displacement of the $E_{1/2}$ [54].

Fig. 6b shows the Koutecky-Levich plots at different rotation speeds which agrees well with the theoretical value for the four-electron transfer process (dashed line), indicating that the ORR proceeds mostly by four-electron transfer to water formation, *i.e.*, $O_2 + 4H^+ + 4e^- \rightarrow 2H_2O$ [55]. Fig. 6c–d shows the experimentally determined potentiodynamic curves of commercial Pt/C and Ni $(OH)_2$@Pt/C-*x*, and Table 1 depicts results of the specific activity ($J_k$) and mass activity ($J_m$) deduced from the polarization curves after normalization. Overall, altering the Ni/Pt composition of the nanoparticles, resulted in significant improvements in the electrochemical performance, yielding up to ~6 times higher mass-normalized specific activity compared to commercial Pt/C.

Fig. 7 displays potentiodynamic stability curves as well as the changes in the normalized electrochemical surface area ECSA (inset) during the 5000 potential cycling scans for commercial Pt/C and Ni$(OH)_2$@Pt/C-*x* samples. The ECSAs decrease as the potential cycling proceeds for all catalysts, however it was more severe for Ni $(OH)_2$@Pt/C-3 and Pt/C samples, which in turn displayed a negative shifting in the ORR potential onset during ORR. Considering the Ni $(OH)_2$@Pt/C-*x* samples, the lowest stability on Ni$(OH)_2$@Pt/C-3 is explained by a severe removal of Ni$(OH)_2$ exposed to the electrolyte. The prior finding was in line with the observation of a small oxidation peak around 0.4 V during the first cycles. On the other hand, Ni$(OH)_2$@Pt/C-6 and Ni$(OH)_2$@Pt/C-12 exhibited better corrosion resistance and hence lower ECSA decreases [10]. Of particular significance is that the ECSA of Ni$(OH)_2$@Pt/C-6 remains virtually unchanged from the first and the 5000th cycle. However, particularly for this sample, considerable increase in the active surface was observed during the first 1000 cycles. Although the specific reason for this is not currently clear, we consider that structural changes occurring during the electrochemical testing by removing the Ni-species with potential cycling exposes further Pt onto the surface and thereby increases the number of actives sites. Similar behavior has been reported elsewhere for comparable systems [10]. A second contribution for improving the stability among Ni$(OH)_2$@Pt/C-*x* might be linked not only to structural conformation and electronic effect (intrinsic bimetallic properties), but also to carbon functionalization. The presence of functional groups on carbon surface enhanced the interaction between nanocatalyst and support, reducing particles mobility and keeping wide dispersion and active surface area [56]. In general, the Ni$(OH)_2$@Pt/C-*x* structures, supported on functionalized carbon exhibited better stability compared to commercial Pt/C.

The elemental composition (i.e. Ni/Pt ratio), showed an important role in tuning the ORR electroactivity and stability. These changes were linked with both geometrical and electronic properties by comparing changes of specific activity ($J_k$) and loss of ECSA with experimental lattice crystal parameters and d-band vacancies (Fig. 8a–b). The contraction of the Pt lattice (Fig. 8a) showed a positive effect on both activity and stability reaching a maximum for the Ni$(OH)_2$@Pt/C-6 sample. The correlation of the electronic structure based on occupancy of d-band vacancies with the catalysts activity and stability showed similar trends, expect in the opposite direction: the d-band vacancies were increased compared with Pt/C (Fig. 8b). The occupancy of d-band vacancies increased in the following sequence: Pt/C< Ni$(OH)_2$@Pt/C-3 < Ni $(OH)_2$@Pt/C-6< Ni$(OH)_2$@Pt/C-12. Increasing the occupancy of d-band vacancies improves the activity and stability, again reaching a maximum for the Ni$(OH)_2$@Pt/C-6 sample. A graphical representation of the catalyst surface structure and the general trends in Pt lattice contraction and d-band occupancies as a function of Pt surface composition are represented in Fig. 8c. These results showed a balance between geometric and electronic parameters, which can clearly modulate the adsorption/desorption properties by increasing or decreasing the bonding energy of adsorbates on Pt. Considering that the ORR involves both the breaking of the O-O bond and the formation of Pt-$OH_{ad}$, which is considered as an ORR reaction inhibitor, changes on Pt parameters will impact the adsorption/desorption energies and ORR reaction kinetics. Multiple studies have demonstrated that a compression of the Pt-lattice positively increases the ORR electroactivity by changing the binding energy of the reaction intermediates (*i.e.* O, OOH and $O_2$) [57–59]. Furthermore, increasing the d-band vacancies facilitates the reaction of adsorbed $OH_{ad}$ to water formation by modifying $\Delta G_{(OHads)}$ [45] and the heat of alloy formation, thus improving the stability with respect to metallic Pt [60]. In addition, we also emphasize the functionalized carbon support plays a substantial factor in stabilization of the nanoparticles, and through improving particle-support interactions we are able to decrease particle agglomeration and maintain high electrochemical surface area.

**Table 1**
Summary of kinetic parameters for the ORR on core-shell NP's with different Ni $(OH)_2$:Pt molar ratios i.e. (Ni$(OH)_2$@$Pt_x$). Commercial Pt/C is shown as reference. X = Ni$(OH)_2$. * OCP recorded in $O_2$-saturated 0.1 M $HClO_4$.

| | Pt/C-Etek | X@Pt/C-3 | X@Pt/C-6 | X@Pt/C-12 |
|---|---|---|---|---|
| ECSA ($m^2\,g^{-1}_{-Pt}$) | 77.1 ± 8.3 | 43.8 ± 11.8 | 51.7 ± 0.35 | 55.9 ± 6.3 |
| $b_o$ ($mV\,dec^{-1}$) | 80.5 ± 6.0 | 56.7 ± 0.2 | 53.5.0 ± 0.7 | 59.0 ± 2.6 |
| $B_o$ ($mA\,cm^{-2}\,rpm^{-1/2}$) | 0.12 ± 0.01 | 0.131 ± 0,01 | 0.135 ± 0.0 | 0.123 ± 0.01 |
| $J_{k0.9V}$ ($mA\,cm^{-2}_{-Pt}$) | 0.21 ± 0.04 | 0.832 ± 0.2 | 1.186 ± 0.11 | 0.697 ± 0.05 |
| $J_{m0.9V}$ ($mA\,mg^{-1}_{-Pt}$) | 0.18 ± 0.04 | 0.329 ± 0.05 | 1.111 ± 0.18 | 0.758 ± 0.17 |
| $E_{1/2}$ (Volts) | 0.88 ± 0.01 | 0.903 ± 0.01 | 0.918 ± 0.01 | 0.926 ± 0.01 |
| OCP (Volts)* | 1.01 ± 0.01 | 1.023 ± 0.017 | 1.035 ± 0.01 | 1.035 ± 0.01 |

### 3.5. Fuel Cell Membrane Electrode Assembly (MEA) Evaluation

Based on the RDE tests, the Ni$(OH)_2$@Pt/C-6 and Ni$(OH)_2$@Pt/C-12 catalysts were selected to investigate their performance within a single membrane electrode assembly fuel cell configuration. The Ni$(OH)_2$@Pt/C-3 catalyst was not tested because of its low stability. Leaching of $Ni^{2+}$ ions can cause issues related to the poisoning of the membrane [61]. The polarization curves were recorded after

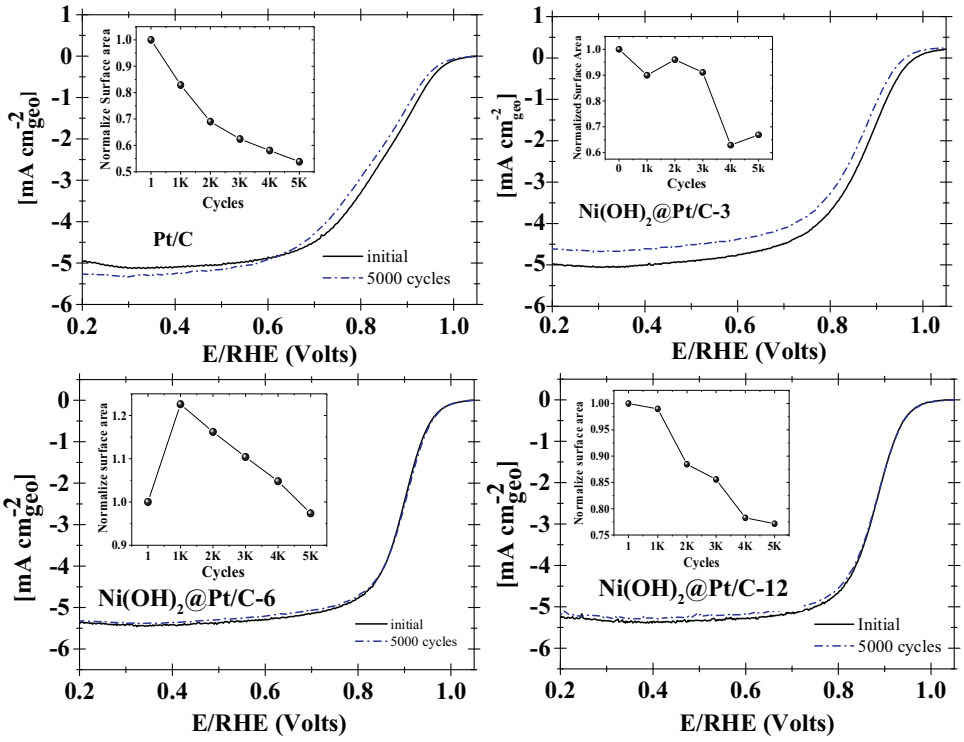


**Fig. 7.** Polarization curves and normalized ECSA degradation of commercial Pt/C-Etek and $Ni(OH)_2$@Pt/C-*x* after stability test, evaluated in a potential range of 0.6 to 1.1 V/RHE, 5000 cycles in 0.1 M $HClO_4$.

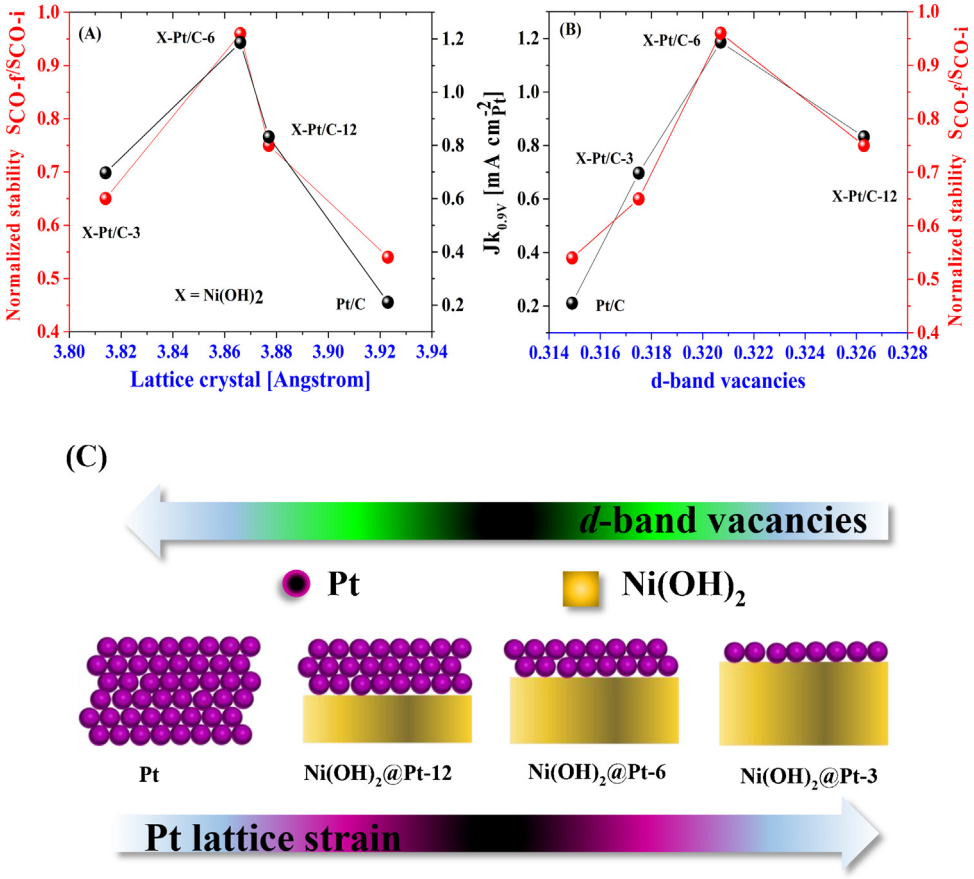


**Fig. 8.** Tendency of both, normalized stability determined by losing of ECSA after 5000 cycles and specific activity at 0.9 V/RHE versus experimental lattice crystal (A), and d-band vacancies obtained by XAS analysis from Pt $L_3$ and $L_2$-edge band (B). Graphical representation of catalyst structure and physicochemical trends (C).

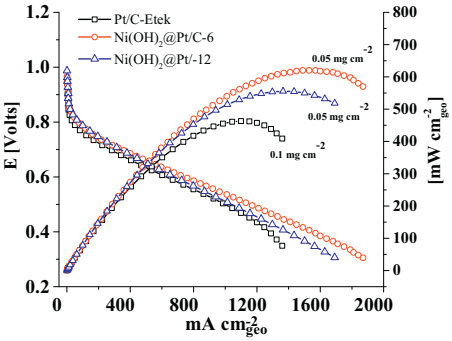


**Fig. 9.** Performance curves from single cells configuration for Pt/C-Etek, $Ni(OH)_2$@Pt/C-6 and $Ni(OH)_2$@Pt/C-12. Conditions: 5 $cm^2$ active area, 80 °C, 20/30 psi anode/cathode, 100%/100% $O_2/H_2$ anode/cathode.

applying a modified break-in protocol at 80 °C, using a stair-like potentiostatic mode [62]. It is important to note that even when similar preparation protocols were carried out, these results represent initial testing of these electrocatalysts in MEA conditions, and further experimental parameter optimization is required in order to improve the performance [63]. Fig. 9 depicts PEMFC polarization curves using single assembly configuration for Pt/C-Etek (0.1 mg $cm^{-2}$), $Ni(OH)_2$@Pt/C-6 and $Ni(OH)_2$@Pt/C-12 (0.05 mg $cm^{-2}$) without iR-drop compensation. Power densities at 0.6 V were 436 mW $cm^{-2}$, 425 mW $cm^{-2}$ and 398 mW $cm^{-2}$, for Ni $(OH)_2$@Pt/C-6 and $Ni(OH)_2$@Pt/C-12 and Pt/C-Etek, respectively. Compared to commercial Pt/C-catalysts, the $Ni(OH)_2$@Pt/C-6 and $Ni(OH)_2$@Pt/C-12 catalysts showed better performance over all current densities as a result of their intrinsically higher ORR activity. Nevertheless, these improvements were not to the same degree as observed by RDE, although is worth emphasizing that only half of the total load was used for the catalysts $Ni(OH)_2$/Pt-*x* versus Pt/C. At high current densities, the commercial Pt/C-Etek showed higher mass-transport losses which might be associated to water flooding likely related to the higher catalyst loading. This issue was lower in the other catalysts.

## 4. Conclusions

Well-defined and highly dispersed $Ni(OH)_2$@Pt/C electrocatalysts with different Pt compositions and supported on functionalized carbon, were synthesized through an straightforward and high-yield process involving sequential chemical reduction using $NaBH_4$ and a transmetallation deposition method. The structures were thoroughly characterized using STEM, HRTEM, SAED, XRD using Rietveld fitting, XAS, and electrochemistry. The experiments support the conclusion that the Pt-Pt bond length is affected by the interaction with $Ni(OH)_2$. As the Pt content deceased, the Pt-Pt distance and the number of d-vacancies per atom also decreased. Based on this finding, the strain ratio and electronic properties could be controlled by the amount of Pt deposited on the $Ni(OH)_2$ core. The $Ni(OH)_2$:Pt ratio significantly affected both the activity and stability. Decreasing the percentage of Pt on $Ni(OH)_2$ promoted higher electrocatalytic properties for the ORR, however an increase in the material instability occurred when the Pt content remained too low. Overall, altering the composition of the Pt shell at the Ni $(OH)_2$ nanoparticle resulted in significant improvements in the electrochemical performance yielding in up to ~6 times higher surface and mass-normalized activity compared to commercial Pt/C. This study shows that Pt surface segregated catalysts with an optimal $Ni(OH)_2$:Pt ratio that maintains Pt on the surface as low as possible to ensure surface coverage provide high activities, improved stability and lower cost than commercial Pt/C. In this regard, a comparison with our best catalysts, only ~6 wt. % Pt phase was used which represents a decrease of ~3 times less Pt compared with commercial Pt/C (20 wt % of Pt). These results have important implications for the design and development of high performance electrocatalysts with ultralow Pt content that have both high activity and extended durability. Electrocatalysts with controlled Pt surface compositions and that can be synthesized using rapid, scalable methods have significant opportunities to provide improved ORR catalysts for fuel cells, metal-air batteries, electrochemical sensors as well as other electrocatalytic processes (*e.g.* hydrogen oxidation, methanol oxidation, carbon monoxide oxidation, *etc.*).

## Acknowledgements

This study was financially supported by the Mexican Council of Science and Technology, CONACYT (grant FOINS/75/2015) and (Grant No. 245920). FGS thanks CONACYT for postdoctoral fellowship. CPR acknowledges support from the National Science Foundation (Grant No. DMR-1205670) and Texas State Universityresearch faculty start-up grant.

## Appendix A. Supplementary data

Supplementary data associated with this article can be found, in the online version, at http://dx.doi.org/10.1016/j.electacta.2017.06.073.

## References

[1] F. Cheng, J. Chen, Metal-air batteries: from oxygen reduction electrochemistry to cathode catalysts, Chem. Soc. Rev. 41 (2012) 2172.
[2] Y. Nie, L. Li, Z. Wei, Recent advancements in Pt and Pt-free catalysts for oxygen reduction reaction, Chem. Soc. Rev 44 (2015) 2168.
[3] W. Vielstich, A. Lamm, H.A. Gasteiger, Handbook of Fuel Cells: Fundamentals, Technology, Applications, Wiley-VCH, 2010.
[4] DoE. Table 3.4.13 Technical targets: Electrocatalysts for Transportation Application. http://www.eere.energy.gov. NEDO, http//www.nedo.go.jp/emglish/index.html (june 2013).
[5] A. Bonnefont, P. Ruvinskiy, M. Rouhet, A. Orfanidi, S. Neophytides, E. Savinova, WIREs Energy Environ (2016) 2014.
[6] M. Fayette, R.D. Robinson, Chemical transformations of nanomaterials for energy applications, J. Mat. Chem. A 2 (2014) 5965.
[7] N. Jung, D.Y. Chung, J. Ryu, S.J. Yoo, Y.E. Sung, Pt-based nanoarchitecture and catalyst design for fuel cell applications, Nano Today 9 (2014) 433.
[8] M. Shao, Q. Chang, J.P. Dodeletand, R. Chenitz, Recent Advances in Electrocatalysts for Oxygen Reduction Reaction, Chemical Review 116 (2016) 3594.
[9] Q. Jia, K. Caldwell, D.E. Ramaker, J.M. Ziegelbauer, Z. Liu, Z. Yu, M. Trahan, S. Mukerhee, In situ spectroscopic evidence for ordered core-shell Pt1Co1 nanoparticles with enhanced activity and stability as oxygen reduction electrocatalysts, J. Phys. Chem. C 118 (2014) 20496.
[10] D. Wang, H.L. Xin, R. Hovden, H. Wang, Y. Yu, D.A. Muller, F.J. DiSalvo, H.D. Abruña, Structurally ordered intermetallic platinum-cobalt core-shell

nanoparticles with enhanced activity and stability as oxygen reduction electrocataysts, Nat. Mat. 12 (2013) 81.
[11] C. Cui, L. Gan, M. Heggen, S. Rudi, P. Strasser, Compositional segregation in shape Pt alloy nanoparticles and their structural behavior during electrocatalysis, Nat. Mat. 12 (2013) 765.
[12] H. Yang, Platinum-based electrocatalysts with core-shell nanostructures, Ang. Chem. Int. Ed 50 (2011) 2674.
[13] H. Yano, M. Kataoka, H. Yamashita, H. Uchida, M. Watanabe, Oxygen Reduction Activity of Carbon-Supported Pt-M (M = V, Ni, Cr, Coand Fe) Alloys Prepared by Nanocapsule Method, Langmuir 23 (2007) 6438.
[14] L. Cao, T. Muller, Rational design of Pt3Ni surface structures for the oxygen reduction reaction, J. Phys. Chem. C 119 (2015) 17735.
[15] G. Ramos-Sanchez, F. Godinez-Salomon, O. Solorza-Feria, P.B. Balbuena, Actinity and durability of PEFCs alloys core-shell catalysts: role of Surface oxidation, Adv. Sci. Tech. 93 (2014) 31.
[16] R.V. Stamenkovic, B.S. Mun, K.J.J. Mayrhofer, P.N. Ross, N.M. Markovic, Effect of Surface Composition on Electronic Structure,Stability, and Electrocatalytic Properties of Pt-Transition Metal Alloys: Pt-Skin versus Pt-Skeleton Surfaces, J. Am. Chem. Soc 128 (2006) 8813.
[17] M. Ahmadi, F. Behafarid, C. Cui, P. Strasser, B.R. Cuenya, Long-Range Segregation Phenomena in Shape-Selected Bimetallic Nanoparticles: Chemical State Effects, ACS Nano 10 (2013) 9195.
[18] J. Gregori, J.J. García-Jareño, D. Giménez-Romero, F. Vicente, Effect of Anions and Oxygen on the Kinetics of the Anodic Dissolution of Nickel, Journal of The Electrochemical Society 153 (2006) B206–B212.
[19] B. Zhang, J. Wu, X. Li, H. Liu, B. Yadian, R.V. Ramanujan, K. Zhou, R. Wu, S. Hao, Y. Huang, Passivation of Nickel Nanoneedles in Aqueous Solution, J. Phys. Chem. C 118 (2014) 9073.
[20] T. Ishizaki, K. Yatsugi, K. Akedo, Effect of Particle Size on the Magnetic Properties of Ni Nanoparticles Synthesized with Trioctylphosphine as the Capping Agent, Nanomaterials 6 (2016) 172.
[21] D.A. Palmer, P. Bénézeth, C. Xiao, D.J. Wesolowski, L.M. Anovitz, Solubility Measurements of Crystalline NiO in Aqueous Solution as a Function of Temperature and pH, J. Solution. Chem. 40 (2011) 680.
[22] A.K. Schuppert, A. Savan, A. Ludwig, K.J.J. Mayrhofer, Potential resolved dissolution of Pt-Cu: A thin-film material library study, Electrochimica Acta 144 (2014) 332.
[23] S. Mezzavilla, C. Baldizzone, A.C. Swertz, N. Hodnik, E. Pizzutilo, G. Polymeros, G.P. Keeley, J. Knossalla, M. Heggen, K.J.J. Mayrhofer, F. Schüth, Structure–Activity–Stability Relationships for Space-Confined $Pt_xNi_y$Nanoparticles in the Oxygen Reduction Reaction, ACS Catal. 6 (2016) 8058.
[24] C. Baldizzone, L. Gan, N. Hodnik, G.P. Keeley, A. Kostka, M. Heggen, P. Strasser, K. J.J. Mayrhofer, Stability of Dealloyed Porous Pt/Ni Nanoparticles, ACS Catal. 5 (2015) 5000.
[25] B.H. Han, C.E. Carlton, A. Kongkanand, R.S. Kukreja, B.R. Theobald, L. Gan, R. O'Malley, P. Strasser, F.T. Wagner, Y. Shao-Horn, Record activity and stability of dealloyed bimetallic catalysts for proton exchange membrane fuel cells, Energy Environ. Sci. 8 (2015) 258.
[26] F. Godinez-Salomon, M. Hallen-Lopez, O. Solorza-Feria, Enhanced electroactivity for the oxygen reduction on Ni@Pt core-shell nanocatalyst, Int. J. Hydro. Energ. 37 (2012) 14902.
[27] H.A. Calderon, C. Kisielowski, P. Specht, B. Barton, F. Godinez-Salomon, O. Solorza-Feria, Maintaining the genuine structure of 2D materials and catalytic nanoparticles at atomic resolution, Micron 68 (2014) 164.
[28] T.M. Grehk, P.O. Nilson, Nuclear instruments and methods in physics research section A: accelerators, spectrometers, detector and associated equipment, 467–468 (2001) 635.
[29] S. Carlson, M. Clausén, L. Gridneva, B. Sommarin, C. Svensson, XAFS experiments at beamline I811MAX-lab synchrotron source,Sweden, J. Synchrotron Rad. 13 (2006) 359.
[30] S. Mukerjee, S. Srinivasan, M.P. Soriaga, J. McBreen, Effect of Preparation Conditions of Pt Alloys on Their Electronic, Structural, and Electrocatalytic Activities for Oxygen Reduction – XRD, XAS, and Electrochemical Studies, J. Phys. Chem. 99 (1995) 4577.
[31] Y. Garsany, O.A. Baturina, K.E. Swider-Lyons, S.S. Kocha, Experimental Methods for Quantifying the Activity of Platinum Electrocatalysts for the Oxygen Reduction Reaction, Anal. Chem 82 (2010) 6321.
[32] K.J.J. Mayrhofer, D. Strmcnik, B.B. Blizanac, V. Stamenkovic, M. Arenz, N.M. Markovic, Measurement of oxygen reduction activities via the rotating disc electrode method: From Pt model surfaces to carbon-supported high surface area catalysts, Electrochim. Acta 53 (2008) 3181.
[33] E. Fabbri, S. Taylor, A. t Rabis, P. Levecque, O. Conrad, R. Kötz, T.J. Schmidt, The Effect of Platinum Nanoparticle Distribution on Oxygen Electroreduction Activity and Selectivity, Chem. Cat. Chem. 6 (2014) 1410.
[34] M. Shao, A. Peles, K. Shoemaker, Electrocatalysis on Platinum Nanoparticles: Particle Size Effect on Oxygen Reduction Reaction Activity, Nano Lett 11 (2011) 3714.
[35] Y. Cheng, H. Zhang, C.V. Varanasi, J. Liu, Highly Efficient Oxygen Reduction Electrocatalysts based on Winged Carbon Nanotubes, Sci. Rep. 3 (2013) 3195.
[36] R.M. Arán-Ais, Y. Yu, R. Hovden, J. Solla-Gullón, E. Herrero, J.M. Feliu, H.D. Abruña, Identical Location Transmission Electron Microscopy Imaging of Site-Selective Pt Nanocatalysts: Electrochemical Activation and Surface Disordering, J. Am. Chem. Soc. 137 (2015) 14992.
[37] G. Ramos-Sanchez, S. Praserthdam, F. Godinez-Salomon, C. Barker, M. Moerbe, H.A. Calderon, L.A. Lartundo, M.A. Leyva, O. Solorza-Feria, P.B. Balbuena, Challenges of modelling real nanoparticles: Ni@Pt electrocatalysts for the oxygen reduction reaction, Phys. Chem. Chem. Phys 17 (2015) 28286.
[38] I.N. Leontyev, A.B. Kuriganova, N.G. Leontyev, L. Hennet, A. Rakhmatullin, N.V. Smirnova, V. Dmitriev, Size Dependence of the Lattice Parameters of Carbon Supported Platinum Nanoparticles: X-ray Diffraction Analysis and Theoretical Considerations, RSC Adv. 4 (2014) 35959.
[39] Y. Zhang, T. Han, J. Fang, P. Xu, X. Li, J. Xu, C.C. Liu, Integrated $Pt_2Ni$ alloy@Pt core–shell nanoarchitectures with high electrocatalytic activity for oxygen reduction reaction, J. Mater. Chem. A 2 (2014) 11400.
[40] R. Ferrando, J. Jellinek, R.L. Johnston, Nanoalloys: from theory to applications of alloy clusters and nanoparticles, Chem Rev 108 (2008) 845.
[41] K.A. Kuttiyiel, K. Sasaki, Y. Choi, D. Su, P. Liu, R.R. Adzic, Nitride Stabilized PtNi Core–Shell Nanocatalyst for high Oxygen Reduction Activity, Nano Lett. 12 (2012) 6266.
[42] S. Koh, P. Strasser, Electrocatalysis on Bimetallic Surfaces: Modifying Catalytic Reactivity for Oxygen Reduction by Voltammetric Surface Dealloying, J. Am. Chem. Soc 129 (2007) 12624.
[43] H. Yu-Chi, Y. Zhang, D. Su, V. Volkov, R. Si, L. Wu, Y. Zhu, W. An, P. Liu, P. He, S. Ye, R.R. Adzic, J.X. Wang, Ordered bilayer ruthenium–platinum core-shell nanoparticles as carbon monoxide-tolerant fuel cell catalysts, Nat. Commun. 4 (2013) 2466.
[44] B. Ravel, M. Newville, ATHENA, ARTEMIS, HEPHAESTUS: data analysis for X-ray absorption spectroscopy using IFEFFIT, J. Synchrotron Rad. 12 (2005) 537.
[45] S. Mukerjee, S. Srinivasan, M.P. Soriaga, J. McBreen, Role of Structural and Electronic Properties of Pt and Pt Alloys on Electrocatalysis of Oxygen Reduction An *In Situ* XANES and EXAFS Investigation, J. Electrochem. Soc 142 (1995) 1409.
[46] T.M. Grehk, P.O. Nilsson, The design of the material science beamline, I811, at MAX-II, Inst. and Meth, Phys. Res. A 467–468 (2001) 635.
[47] S. Henning, L. Kühn, J. Herranz, J. Durst, T. Binninger, M. Nachtegaal, M. Werheid, W. Liu, M. Adam, S. Kaskel, A. Eychmüller, T.J. Schmidt, Pt-Ni Aerogels as Unsupported Electrocatalysts for the Oxygen Reduction Reaction, J. Electrochem. Soc 163 (2016) F998.
[48] A.E. Sanlı, A. Aytaç, Electrochemistry of the Nickel Electrode as a Cathode Catalyst in the Media of Acidic Peroxide for Application of the Peroxide Fuel Cell, ECS Trans. 42 (2012) 3.
[49] P. Mani, R. Srivastava, P. Strasser, Dealloyed Pt-Cu Core-Shell Nanoparticle Electrocatalysts for Use in PEM Fuel Cell Cathodes, J. Phys. Chem. C 112 (2008) 2770.
[50] C. Wang, M. Chi, D. Li, D. Strmcnik, D. van der Vliet, G. Wang, V. Komanicky, K.C. Chang, A.P. Paulikas, D. Tripkovic, J. Pearson, K.L. More, N.M. Markovic, V.R. Stamenkovic, Design and Synthesis of Bimetallic Electrocatalyst with Multilayered Pt-Skin Surfaces, J. Am. Chem. Soc. 133 (2011) 14396.
[51] N.M. Marković, P.N. Ross Jr., Surface science studies of model fuel cell electrocatalysts, Surf. Sci. Rep. 45 (2002) 117.
[52] V.R. Stamenkovic, B. Fowler, B.S. Mun, G. Wang, P.N. Ross, C.A. Lucas, N.M. Marković, Improved oxygen reduction activity on Pt3Ni(111) via increased surface site availability, Science 315 (2007) 493.
[53] H.A. Gasteiger, S.S. Kocha, B. Sompalli, F.T. Wagner, Activity benchmarks and requirements for Pt,Pt-alloy, and non-Pt oxygen reduction catalysts for PEMFCs, Appl. Catal. B Environ. 56 (2005) 9.
[54] N. Alonso-Vante, Platinum and Non-Platinum Nanomaterials for the Molecular Oxygen Reduction Reaction, Chem. Phys. Chem 11 (2010) 2732.
[55] J.L. Reyes-Rodríguez, F. Godínez-Salomón, M.A. Leyva, O. Solorza-Feria, RRDE study on Co@Pt/C core–shell nanocatalysts for the oxygen reduction reaction, Int. J. Hydro. Ener. 38 (2013) 12634.
[56] L.T. Soo, K.S. Loh, A.B. Mohamad, W.R. Wan Daud, W.Y. Wong, An overview of the electrochemical performance of modified graphene used as an electrocatalyst and as a catalyst support in fuel cells, App. Catal. A: General 497 (2015) 198.
[57] G.E. Ramírez-Caballero, Y. Ma, R. Callejas-Tovar, P.B. Balbuena, Surface segregation and stability of core–shell alloy catalysts foroxygen reduction in acid medium, Phys. Chem. Chem. Phys. 12 (2010) 2209.
[58] P. Strasser, S. Koh, T. Anniyev, J. Greeley, K. More, C. Yu, Z. Liu, S. Kaya, D. Nordlund, H. Ogasawara, M.F. Toney, A. Nilsson, Lattice-strain control of the activity in dealloyed core-shell fuel cell catalysts, Nat Chem. 6 (2010) 454.
[59] N.B. Wanjala, R. Loukrakpam, J. Luo, P.N. Njoki, D. Mott, C.J. Zhong, M. Shao, L. Protsailo, T. Kawamura, Thermal Treatment of PtNiCo Electrocatalysts: Effects of Nanoscale Strain and Structure on the Activity and Stability for the Oxygen Reduction Reaction, J. Phys. Chem. C 114 (2010) 17580.
[60] S.J. Hwang, S.K. Kim, J.G. Lee, S.C. Lee, J.H. Jang, P. Kim, T.H. Lim, Y.E. Sung, S.J. Yoo, Role of Electronic Perturbation in Stability and Activity of Pt-Based Alloy Nanocatalysts for Oxygen Reduction, J. Am. Chem. Soc. 134 (2012) 19508.
[61] J. Durst, M. Chatenet, F. Maillard, Impact of metal cations on the electrocatalytic properties of Pt/C nanoparticles at multiple phase interfaces, Phys. Chem. Chem. Phys 14 (2012) 13000.
[62] X.Z. Yuan, S. Zhang, J.C. Sun, H. Wang, A review of accelerated conditioning for a polymer electrolyte membrane fuel cell, J. Pow. Sources 196 (2011) 9097.
[63] P. Mani, R. Srivastava, P. Strasser, Dealloyed binary $PtM_3$ (M = CuCo,Ni) and ternary $PtNi_3M$ (M = Cu,Co,Fe,Cr) electrocatalysts for the oxygen reduction reaction: Performance in polymer electrolyte membrane fuel cells, J. Pow Sources 196 (2011) 666.